Journal of Materials Chemistry C

ROYAL SOCIETY OF CHEMISTRY

PAPER

View Article Online
View Journal | View Issue

Published on 29 June 2020. Downloaded by East China Normal University on 8/25/2020 1:25:02 PM.

Cite this: J. Mater. Chem. C, 2020, 8, 11160

# Enhanced carrier separation in ferroelectric $In_2Se_3/MoS_2$ van der Waals heterostructure†

Bin Zhou,[a] Kai Jiang,[a] Liyan Shang,[a] Jinzhong Zhang,[a] Yawei Li,[a] Liangqing Zhu,[a] Shi-Jing Gong,*[b] Zhigao Hu*[acd] and Junhao Chu[acd]

Received 17th May 2020, Accepted 29th June 2020

DOI: 10.1039/d0tc02366c

rsc.li/materials-c

α-$In_2Se_3$, a recently reported two-dimensional (2D) van der Waals (vdW) ferroelectric, is gaining significant attention due to its potential applications in nano-scale devices. Here, we have systematically investigated the electronic properties of three configurations of $In_2Se_3/MoS_2$(I, II, III) heterostructures by first-principles calculations. The results reveal that the intrinsic ferroelectricity polarization in α-$In_2Se_3$ can dramatically tune the electronic properties. When the out-of-plane ferroelectric polarization field is pointing from $In_2Se_3$ towards $MoS_2$, the energy band of the heterostructure is type-II band alignment with a band gap of 0.8 eV, which is beneficial for carrier separation. With reversal of the ferroelectric polarization, the band alignment switches from type-II to type-I with a band gap of 1.6 eV, which is suitable for luminescence device applications. Based on the nonequilibrium Green's function method (NEGF), the calculated photoinduced current density under visible-light radiation is up to ~0.5 mA cm$^{-2}$ in the $In_2Se_3/MoS_2$(I) heterostructure, which can remarkably exceed that of thin-film silicon devices at a phonon energy below 2.5 eV. Moreover, the band alignment transition can also be realized through the application of an external electric field. We believe that the present work will greatly enlarge the potential applications of the $In_2Se_3$-based heterostructures in future nano-optoelectronic devices.

## 1 Introduction

Two-dimensional (2D) materials, which exhibit diverse electronic properties ranging from insulating and semiconducting to semimetallic, have boosted the development of nanoelectronics in the past decades.[1–5] A large number of 2D materials such as silicene, stanene and transition metal dichalcogenides (TMDC) have been implemented in field effect transistors (FETs) and optoelectronic applications. Recently, emerging 2D ferroelectric polarization materials in the form of $III_2$–$VI_3$ have been proposed and confirmed in experimental aspects (*e.g.*, α-$In_2Se_3$).[6–9] It is reported that α-$In_2Se_3$ possesses robust intrinsically out-of-plane ferroelectric polarization. Due to its switchable ferroelectric polarization, α-$In_2Se_3$ exhibits a memristive behavior, which is promising for data storage applications. Moreover, the spontaneous ferroelectric polarization can be reversed through laterally shifting the central Se layer, thus, it provides a platform for exploring nonvolatile ferroelectric switches and memory devices.

Additional, the newly explored van der Waals (vdW) heterostructures, which are composed of two or more different 2D materials, have played an important role in investigating fundamental physical phenomena and designing functional devices.[10–14] In particular, ferroelectric $In_2Se_3$ based vdW heterostructures have attracted a great deal of attention recently. Wan *et al.*[15] reported a ferroelectric diode fabricated from graphene and α-$In_2Se_3$ layers with an on/off ratio of up to ~$10^5$. Jiang *et al.*[16] reported that an $In_2Se_3/MoS_2$ heterostructures based photoanode is beneficial for photoelectrochemical water splitting. Kang *et al.* theoretically demonstrated the possibility of 2D ferroelectric tunnel junctions constructed with graphene and α-$In_2Se_3$, which show excellent tunnel electroresistance (TER) effects with TER ratios up to $1 \times 10^8$%.[17] These studies show that 2D ferroelectric-based vdW heterostructures are considered to be promising in next generation tunable nanoelectronic devices.

In this work, we construct $In_2Se_3/MoS_2$ heterostructures with different ferroelectric polarization directions. The intrinsic electric field tunability of interface properties and the enhanced light absorption and large photocurrent density in the $In_2Se_3/MoS_2$

[a] *Technical Center for Multifunctional Magneto-Optical Spectroscopy (Shanghai), Engineering Research Center of Nanophotonics & Advanced Instrument (Ministry of Education), Department of Materials, School of Physics and Electronic Science, East China Normal University, Shanghai 200241, China. E-mail: zghu@ee.ecnu.edu.cn; Fax: +86-21-54342933; Tel: +86-21-54345150*

[b] *Key Laboratory of Polar Materials and Devices (MOE), East China Normal University, Shanghai 200241, China. E-mail: sjgong@ee.ecnu.edu.cn*

[c] *Collaborative Innovation Center of Extreme Optics, Shanxi University, Taiyuan, Shanxi 030006, China*

[d] *Shanghai Institute of Intelligent Electronics & Systems, Fudan University, Shanghai 200433, China*

† Electronic supplementary information (ESI) available. See DOI: 10.1039/d0tc02366c



This journal is © The Royal Society of Chemistry 2020

Published on 29 June 2020. Downloaded by East China Normal University on 8/25/2020 1:25:02 PM.

heterostructure are revealed. Besides, the electronic properties of the $In_2Se_3/MoS_2$ can be effectively modulated by applying an external electric field. It is believed that these theoretical findings will open up new possibilities for designing novel tunable nanoelectronic devices based on 2D ferroelectric vdW heterostructures.

## 2 Computational details

All the calculations are performed by using the Vienna *ab initio* simulation package (VASP).[18–20] The interaction between the core and valence electrons is described using the projector-augmented wave (PAW) method. Here the Perdew–Burke–Ernzerhofer (PBE) exchange–correlation potential functional within the generalized gradient approximation (GGA) is employed.[21,22] The interlayer interactions in the $In_2Se_3/MoS_2$ vdW heterostructures are considered by adopting the semi-empirical DFT-D3 method to describe long-range vdW interactions.[23] Meanwhile, the energy cut off of 500 eV is used for the plane wave expansion. The $5 \times 5 \times 1$ *k*-points are sampled for the correlative monolayer and heterostructures.[24] All the structures are fully relaxed until the force on each atom is smaller than 0.05 eV $Å^{-1}$, and the total energy convergence criterion is set as $10^{-6}$ eV. Moreover, a vacuum region of 20 Å is chosen to prevent artificial interactions between neighboring sheets along the $z$ direction. As the GGA-PBE is known to underestimate the band gap of semiconductors, the HSE06 method with the mixing exchange parameter of 0.25 and screening parameter of 0.2 $Å^{-1}$ are employed for a more accurate band gap and optical absorption calculation.

The optical absorption properties in $In_2Se_3/MoS_2$ heterostructures are explored. The absorption range of the spectrum is determined by the optical absorption coefficients. Based on the frequency-dependent dielectric function, the optical absorption coefficient $\alpha(\omega)$ can be calculated using the formula:

$$\alpha(\omega) = \sqrt{2}\omega\left[\sqrt{\varepsilon_1(\omega)^2 + \varepsilon_2(\omega)^2} - \varepsilon_1(\omega)\right]^{1/2} \tag{1}$$

where $\varepsilon_1$ and $\varepsilon_2$ are the real part and imaginary parts of the complex dielectric function, respectively.

Furthermore, the photocurrent density is calculated based on the nonequilibrium Green's function-DFT method, as implemented in Quantum ATK software.[25] This method takes into consideration the electron–photon interaction on the device Hamiltonian, using first-order perturbation theory, where the detailed descriptions of this method can be found in the previous studies,[26–29] and is given by

$$I_\alpha = \frac{e}{h}\int_{-\infty}^{\infty}\sum_{\beta=L,R}[1-f_\alpha(E)]f_\beta(E-\hbar\omega)T^{-}_{\alpha,\beta}(E) - f_\alpha(E)[1-f_\beta(E+\hbar\omega)]T^{+}_{\alpha,\beta}(E)\mathrm{d}E \tag{2}$$

$$T^{-}_{\alpha,\beta}(E) = N\mathrm{Tr}\{M^\dagger\tilde{A}_\alpha(E)MA_\beta(E-\hbar\omega)\} \tag{3}$$

$$T^{+}_{\alpha,\beta}(E) = N\mathrm{Tr}\{M\tilde{A}_\alpha(E)M^\dagger A_\beta(E+\hbar\omega)\} \tag{4}$$

where $f$ is the Fermi–Dirac distribution function of electrode $\alpha$ ($\alpha \in L, R$), $A_\alpha = G\Gamma_\alpha G^\dagger$ is the spectral function of electrode $\alpha$, $G$ and $G^\dagger$ are the retarded and advanced Green's functions, respectively. The electron–photon coupling matrix is given by

$$M_{\mathrm{ml}} = \frac{e}{m_0}\left(\frac{\hbar\sqrt{\tilde{\mu}_\mathrm{r}\tilde{\varepsilon}_\mathrm{r}}}{2N\omega\tilde{\varepsilon}c}F\right)^{1/2}\mathbf{e}\cdot\mathbf{P}_{\mathrm{ml}} \tag{5}$$

The total photocurrent is the current discrepancy between the two electrodes. $\Gamma_\alpha$ is the spectral broadening, and the momentum operator $\mathbf{P}_{\mathrm{ml}}$ is calculated using the nonequilibrium Green's function (NEGF) method.

## 3 Results and discussion

### 3.1 Polarization tuning effects on electronic properties of $In_2Se_3/MoS_2$ vdW heterostructures

Before constructing the $In_2Se_3/MoS_2$ vdW heterostructures, we firstly investigate the geometric structures of $MoS_2$ and $In_2Se_3$. The $MoS_2$ monolayer has a hexagonal structure with the intralayer atoms sandwiched in the order of S–Mo–S. The optimized lattice constants for $MoS_2$ are $a = b = 3.18$ Å. The structure of $\alpha$-$In_2Se_3$ possesses a hexagonal lattice with the five atoms stacking in the sequence of Se–In–Se–In–Se. The calculated lattice constants for the $\alpha$-$In_2Se_3$ monolayer are $a = b = 4.09$ Å. In order to minimize the lattice mismatch value of the constructed heterostructures, we adopt a $4 \times 4$ $MoS_2$ and a $3 \times 3$ $In_2Se_3$ supercell to construct the $In_2Se_3/MoS_2$ vdW heterostructures. The lattice mismatch is less than 2%, and the strain effects on the electronic properties are very little and can be neglected. We present the band structures of $3 \times 3$ $\alpha$-$In_2Se_3$, $4 \times 4$ $MoS_2$ monolayers, as shown in Fig. S1 (ESI†). The results show that the $\alpha$-$In_2Se_3$ monolayer has an indirect band gap of 0.78 eV by PBE (1.65 eV by HSE06), while the $MoS_2$ monolayers possess a direct band gap of 1.83 eV by PBE (2.15 eV by HSE06), as listed in Table 1, which are in good agreement with the previous results.[6,30,31]

Based on different ferroelectric polarization directions of the $In_2Se_3$ layer, three different stacking configurations (labeled as I, II and III) are conceived to construct the $In_2Se_3/MoS_2$ heterostructures, as shown in Fig. 1. In the configuration I, the center Se atoms are close to the interface, in which the out-of-plane intrinsic polarization $P$ deviates from $MoS_2$. For configuration III, the polarization $P$ is reversed. In the configuration II, which is an intermediate state, the central Se atoms are almost located in the middle of the $In_2Se_3$ layer. In order to quantitatively characterize the stability of $In_2Se_3/MoS_2$(I, II, III), the binding

Table 1 Calculated equilibrium interlayer distance $d_0$ (Å), binding energy $E_b$ (meV) (per atom), work function $W$ (eV), band gaps (eV) (PBE/HSE06), and potential difference $\Delta\Phi$ (eV) for three configurations

| | $d_0$ | $E_b$ | $W$ | $E_g^{PBE}$ | $E_g^{HSE06}$ | $\Delta\Phi$ |
|---|---|---|---|---|---|---|
| $MoS_2$ | | | 5.34 | 1.83 | 2.15 | 0 |
| $\alpha$-$In_2Se_3$ | | | 5.99 | 0.78 | 1.65 | 1.34 |
| I | 3.22 | −60.27 | 5.77 | 0.35 | 0.81 | 1.04 |
| II | 3.33 | −56.26 | 5.72 | 1.00 | 1.58 | 0.43 |
| III | 3.37 | −56.50 | 6.04 | 0.81 | 1.62 | 1.16 |

Published on 29 June 2020. Downloaded by East China Normal University on 8/25/2020 1:25:02 PM.

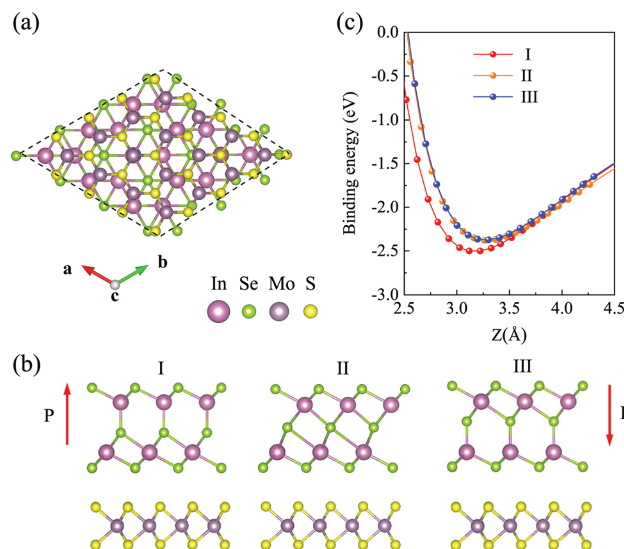


Fig. 1 (a) and (b) Top and side views of $In_2Se_3/MoS_2$(I, II, III) heterostructures. (c) The calculated binding energies as a function of the interlayer distance for the corresponding $In_2Se_3/MoS_2$ heterostructures. The red arrows indicate the direction of the out-of-plane spontaneous electric polarization in $In_2Se_3$.

energies as a function of the interlayer distances are shown in Fig. 1(c), which is defined as

$$E_b = E_{In_2Se_3/MoS_2} - (E_{In_2Se_3} + E_{MoS_2}) \quad (6)$$

where $E_{In_2Se_3/MoS_2}$ is the total energy of the $In_2Se_3/MoS_2$ vdW heterostructure, $E_{In_2Se_3}$ and $E_{MoS_2}$ are the total energy of an isolated $In_2Se_3$ and $MoS_2$ monolayer, respectively. Typical vdW equilibrium distances of 3.22 Å, 3.33 Å and 3.37 Å were obtained for $In_2Se_3/MoS_2$(I), $In_2Se_3/MoS_2$(II) and $In_2Se_3/MoS_2$(III), respectively. As shown in Table 1, the calculated binding energies $E_b$ are −60.27, −56.26 and −56.50 meV per atom, respectively, which are closer to the calculated interlayer binding energy of an $In_2Se_3$ bilayer (−56.20 meV per atom).[6] Therefore, $In_2Se_3$ and $MoS_2$ monolayers can form considerably stable 2D vdW heterostructures. It is noted that the configuration I has a more negative binding energy, as compared to the other two configurations. This is because in $In_2Se_3/MoS_2$(I) the intrinsic electric field $E$ induced in the $In_2Se_3$ layer is equal to the direction of the interfacial built-in electric field, which can enhance and facilitate the electron transfer from $MoS_2$ to the $In_2Se_3$ layer, and lead to a stronger vdW interaction.

Fig. 2 shows the projected band structures and band alignments of the $In_2Se_3/MoS_2$(I, II, III) heterostructures. For $In_2Se_3/MoS_2$(I, II, III), the band gap is calculated to be about 0.35 eV, 1.0 eV and 0.81 eV by PBE (0.81 eV, 1.58 eV and 1.62 eV by HSE06, see Fig. S2 in the ESI†) respectively, as listed in Table 1. It is found that the band structures of the three $In_2Se_3/MoS_2$ heterostructures are not a simple superposition of the two monolayers, their band structures are influenced by the ferroelectric polarization field. In configuration I, it is clear that the conduction band minimum (CBM) of the band structure is

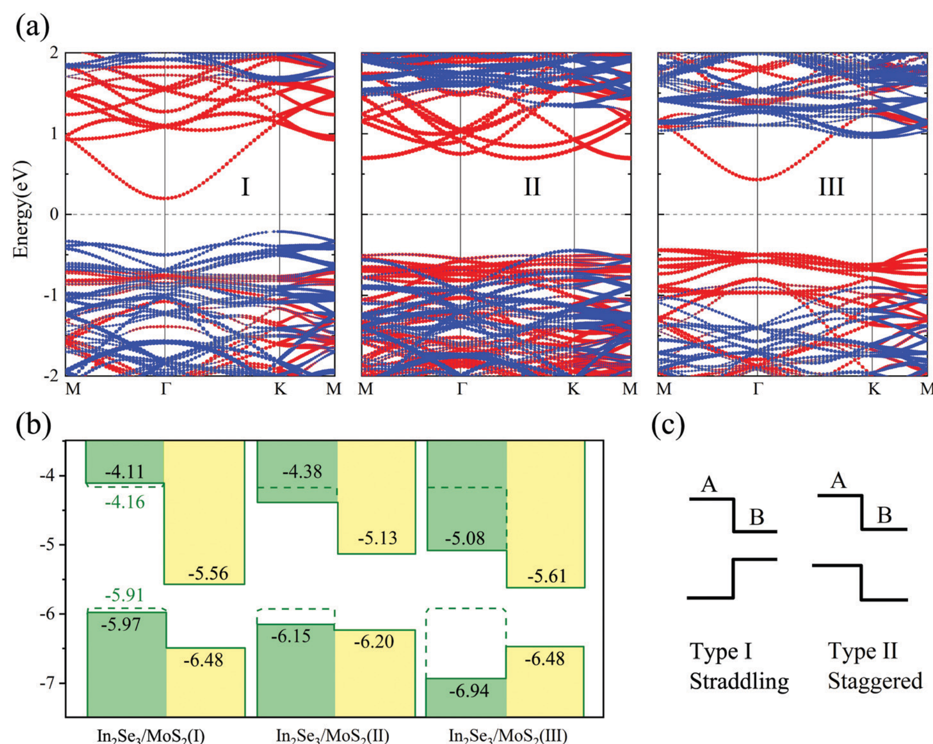


Fig. 2 (a) The projected band structures for $In_2Se_3/MoS_2$(I, II, III) heterostructures based on PBE calculations. The red and blue dots represent the contributions from $In_2Se_3$ and $MoS_2$, respectively. The Fermi level is set as zero. (b) Band edge alignments of the vdW heterostructures, where green and yellow represent $MoS_2$ and $In_2Se_3$. The corresponding band edge positions of independent pristine $MoS_2$ are shown by dotted green lines. The vacuum level is taken as the zero reference. (c) The schematic illustration of different band alignment types of $In_2Se_3/MoS_2$ vdW heterostructures.


This journal is © The Royal Society of Chemistry 2020

Published on 29 June 2020. Downloaded by East China Normal University on 8/25/2020 1:25:02 PM.

dominated by the $In_2Se_3$ layer, while the valence band minimum (VBM) is contributed by the $MoS_2$ layer. Thus, the $MoS_2$ layer can be used as the electron donor and the $In_2Se_3$ layer can be used as the electron acceptor for the separation of carriers. Such a band alignment can greatly improve the electron–hole separation efficiency, leading to a low electron–hole recombination efficiency. For $In_2Se_3/MoS_2$(II), the polarization electric field in $In_2Se_3$ is weakened and a quasi type-II band alignment is displayed. When the polarization electric field of $In_2Se_3$ is reversed from a downward to upward direction, it becomes the case of configuration III. The band structure displays a typical type-I band alignment characteristic, in which both the CBM and VBM are contributed by the $In_2Se_3$ layer. Thus, the photo-excited electrons and holes can be localized inside the $In_2Se_3$ layer, which promotes the electron and hole recombination rate and the luminescence strength. The configuration III $In_2Se_3/MoS_2$ heterostructure provides an opportunity to realize the type-I band alignment and luminescence device applications.[32] Furthermore, we calculated their projected densities of states (PDOS) between −2 eV and 3 eV to analyze the electronic structures of the $In_2Se_3/MoS_2$(I, II, III) heterostructures, as shown in Fig. S2(a and b) (see ESI†). Comparing the PDOS calculated using PBE and HSE06 methods, we clearly see that HSE06 only corrects band gap values, while the band alignment characteristics determined by the two functionals are almost the same.

In the process of polarization reversal, it can be seen that the energy band of $MoS_2$ moves downward rapidly relative to the band of pristine monolayer $MoS_2$, as shown in Fig. 2(b), which implies that the polarization electric field induced by α-$In_2Se_3$ has an external electric field-like tuning effect on the electronic properties. It was reported that the polarization induced intrinsic electric field $E$ can reach 1 GV $m^{-1}$,[33] which is even higher than the external electric field applied in laboratory conditions. Thus, the controllable separation of carriers can be achieved through adjusting the intrinsic polarization of the $In_2Se_3$ layer. The different band alignments for the three stacking configurations can be mainly attributed to the different internal ferroelectric electric field across the heterostructures. Fig. S3 (ESI†) shows the plane-averaged electrostatic potential along the stacking direction for the three configurations. The electrostatic potential differences between the $MoS_2$ layer and $In_2Se_3$ layer are 1.04 eV for $In_2Se_3/MoS_2$(I), 0.43 eV for $In_2Se_3/MoS_2$(II) and 1.16 eV for $In_2Se_3/MoS_2$(III). As the $In_2Se_3$ and $MoS_2$ formed heterostructures, in the reversal of ferroelectric polarization, the ferroelectric electric field across the heterostructure interface first decreased to zero, then it is reversed. Hence, under the influence of the ferroelectric field, the energy band of $MoS_2$ moves downward gradually, which formed different band alignments in the three stacking configurations.

Interestingly, it is found that the band edge of $MoS_2$ in the configuration I heterostructure deviates little from the corresponding isolated pristine $MoS_2$ layer, while in configuration III, the energy band of $MoS_2$ shifts downward about 1 eV. It indicates

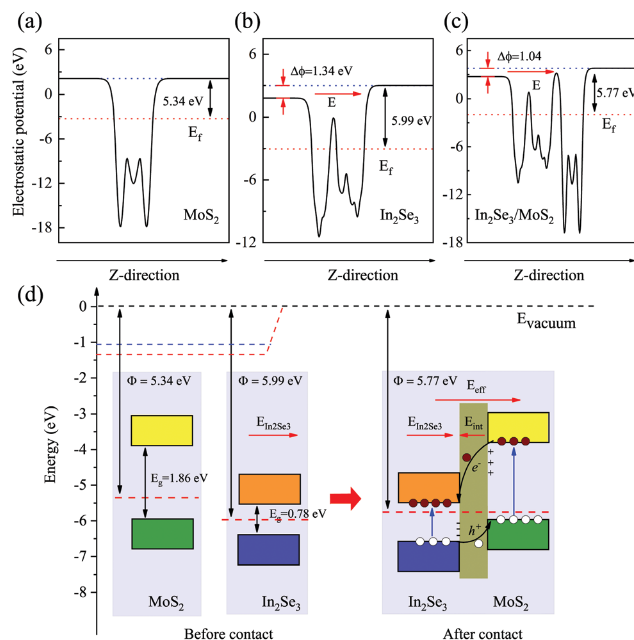


Fig. 3 The electrostatic potentials for the (a) $MoS_2$ monolayer, (b) α-$In_2Se_3$ and (c) $In_2Se_3/MoS_2$(I) heterostructure; the blue and red dotted lines represent the vacuum level $E_0$ and the Fermi level $E_f$, respectively. (d) A schematic diagram of the band configuration and the charge separation at the interface of the $In_2Se_3/MoS_2$(I) heterostructure. $E_{In_2Se_3}$, $E_{int}$ and $E_{eff}$ represent the $In_2Se_3$ induced electric field, the built-in field and net effective electric field crossing the heterostructure, respectively.

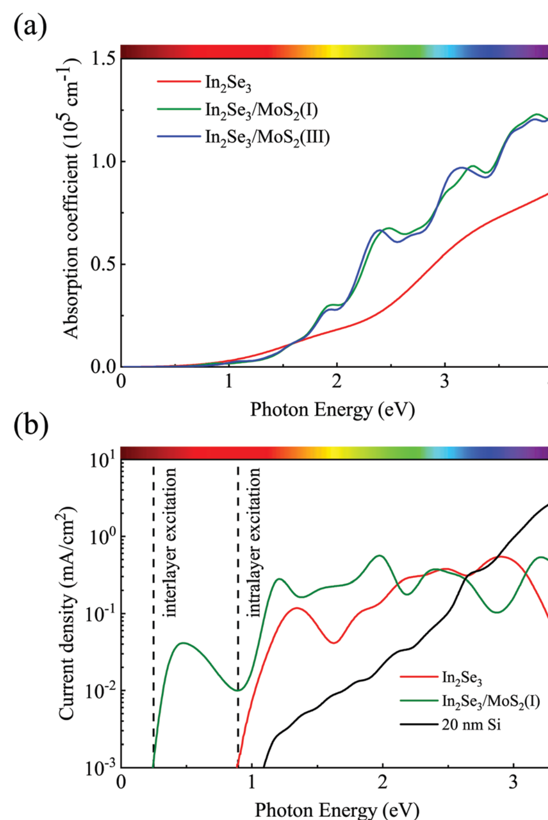


Fig. 4 (a) The optical absorption of the $In_2Se_3/MoS_2$(I, III) heterostructures and the isolated $In_2Se_3$ monolayer. (b) Photocurrent density as a function of photon energy for the $In_2Se_3/MoS_2$(I) heterostructure, monolayer $In_2Se_3$ as well as a 20 nm silicon thin film. The current density was calculated under illumination by an AM 1.5 standard solar spectrum with a photon flux 1 $Å^{-2}$ $s^{-1}$.

Published on 29 June 2020. Downloaded by East China Normal University on 8/25/2020 1:25:02 PM.

that a large energy band shift of $MoS_2$ induced by the polarization electric field happens for the III configuration, which leads to the transformation of type-II to type-I band alignment. For α-$In_2Se_3$, however, the band edge positions in configuration I and III deviate little. This is mainly because the $MoS_2$ monolayer is much more easily influenced by the external electric field compared with the $In_2Se_3$ monolayer.[34,35] It shows that $In_2Se_3$ serves as a good ferroelectric electric field source in the $In_2Se_3/MoS_2$ heterostructure system. Moreover, the Bader charge analysis[36–38] was performed, which shows that there are 0.101 and 0.097 electrons transferred from the $MoS_2$ layer to the $In_2Se_3$ layer for configuration I and configuration III, respectively. It indicates that the $In_2Se_3$ layer becomes an n-doping semiconductor and $MoS_2$ becomes a p-doping semiconductor. Note that this charge redistribution induces a built-in electric field in the interface, which can hinder the diffusion of electrons and holes. The ferroelectric tunable effects have also been revealed in other heterostructure systems, such as $In_2Se_3$/graphene, graphene/GeS, $In_2Se_3/In_2Te_3$.[39] In this work, however, the intrinsic ferroelectric tunability of the separation of carriers is investigated for the $In_2Se_3/MoS_2$ heterostructures system and the enhanced carrier separation mechanism is revealed.

### 3.2 Band alignment and charge transfer mechanism

To further clarify the influence of intrinsic polarization on the electronic properties of the $In_2Se_3/MoS_2$ heterostructure, we presented electrostatic potentials and band alignment of $In_2Se_3/MoS_2$(I), using the vacuum level as a common energy reference, as shown in Fig. 3. The work function is a critical parameter to characterize a material, which can help us to get a further understanding on the origin of the charge transfer mechanism at the heterostructure interface. The work function is defined as follows

$$\Phi = E_{\text{vac.}} - E_{\text{F}} \tag{7}$$

where $E_{\text{vac.}}$ is the energy level of a stationary electron in the vacuum, $E_{\text{F}}$ represents the Fermi level of the corresponding systems. Based on eqn (7), the work functions of the $MoS_2$ monolayer, α-$In_2Se_3$ monolayer and $In_2Se_3/MoS_2$(I) heterobilayer are 5.34, 5.99 and 5.77 eV, respectively, as shown in Fig. 3(a–c). For α-$In_2Se_3$, the electrostatic potential difference between two surfaces is $\Delta\phi$ = 1.34 eV, in which an internal electric field can be self-introduced according to the following equation[40]

$$E_{\text{eff}} = \frac{\Delta\phi}{ed} \tag{8}$$

where, $d$ is the thickness of the heterostructure. Thus, to induce a sizable effective electric field $E_{\text{eff}}$, $d$ should be small enough, *e.g.*, a few nanometers. As shown in Fig. 3(c), after forming the heterostructure, the electrostatic potential difference between the $MoS_2$ layer and $In_2Se_3$ layer is 1.04 eV for configuration I, which can induce an internal intrinsic electric field across the junction. Moreover, it is found that the electrostatic potential difference

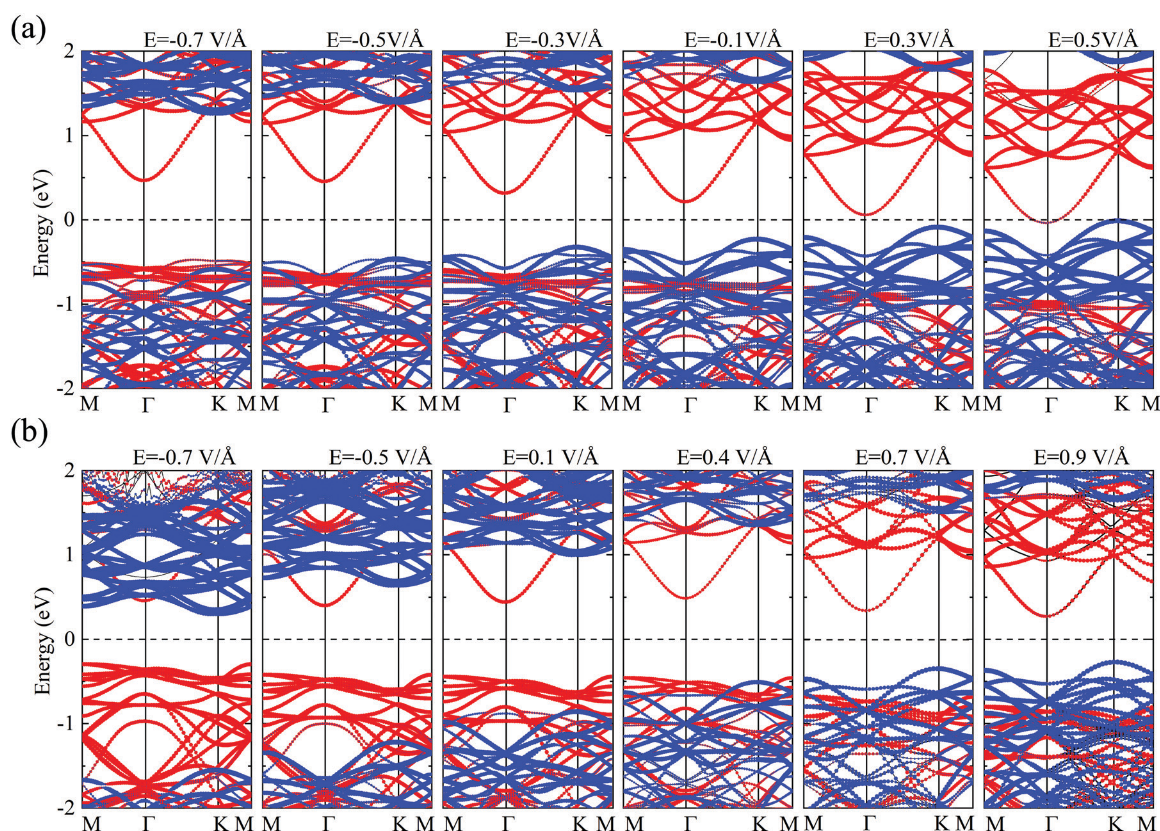


Fig. 5 Evolution diagram of the projected band structure under the influence of different external electric fields for (a) $In_2Se_3/MoS_2$(I) heterostructure and (b) $In_2Se_3/MoS_2$(III) heterostructure.


This journal is © The Royal Society of Chemistry 2020

Published on 29 June 2020. Downloaded by East China Normal University on 8/25/2020 1:25:02 PM.

between $MoS_2$ and $In_2Se_3$ in configuration I is smaller than that of configuration III (1.16 eV, see Fig. S3 in the ESI†). This can be attributed to counteraction of the opposite direction of the built-in electric field induced by the charge transfer at the I interface and the intrinsic ferroelectric field produced by $In_2Se_3$.

After forming the $In_2Se_3/MoS_2$(I) contact, the electrons in $MoS_2$ with a low work function flow into $In_2Se_3$ with a high work function, as shown in Fig. 3(d). Thus, the $In_2Se_3$ layer will accumulate negative charges, while the $MoS_2$ layer will gather positive holes. Finally, the two Fermi levels will reach the same level and the spontaneous interfacial charge transfer will further lead to the formation of an interfacial built-in electric field $E_{int}$ with direction pointing from the $MoS_2$ layer to the $In_2Se_3$ layer. The $E_{int}$ will hinder the diffusion of electrons and holes and the system will finally achieve balance with the diffusion force. However, for the polar system, the opposite intrinsic electric field produced in the $In_2Se_3$ layer will offset the $E_{int}$ and lead to a net effective electric field $E_{eff}$ across the heterostructure. As a result, the $E_{eff}$ produced in the heterostructure could effectively enhance carrier separation in the $In_2Se_3/MoS_2$(I) heterostructure and inhibit the recombination of photo-generated $e^-/h^+$ pairs.

### 3.3 Optical properties and photoexcited current

Next we explored the optical properties of the isolated $In_2Se_3$ monolayers and $In_2Se_3/MoS_2$(I, III) heterostructures. The optical absorption coefficient $\alpha(\omega)$ is calculated based on the formula (1). The obtained optical absorption coefficients of the monolayer and the heterostructures are presented in Fig. 4(a) calculated by using PBE (Fig. S4 in the ESI† by HSE06). The optical absorption coefficients of the I and III heterostructures all display an obvious enhancement, as compared with the isolated $In_2Se_3$ layer. The absorption range is broad from the visible to the ultraviolet light region. We further investigate the optoelectronic device performance of $In_2Se_3/MoS_2$(I). The photon energy dependence of current density is evaluated under standard test conditions (*i.e.*, AM 1.5 spectral illumination of 1000 W $m^{-2}$), which is plotted in Fig. 4(b). For $In_2Se_3$ monolayers, the photocurrents are zero until the photon energy is up to $\sim$0.8 eV, which is consistent with the band gap calculated by PBE. For the $In_2Se_3/MoS_2$(I) heterostructure, the photocurrent density increased rapidly when the photon energy reached about 0.3 eV, which agrees well with the calculated band gap above by PBE. This photocurrent originates from interlayer excitations,[41] in which the conduction band and valence band are in different layers of the heterostructure, effectively reducing the transport gap of the $In_2Se_3/MoS_2$ device. The calculated photo-induced current density under the visible-light radiation is up to 0.5 mA $cm^{-2}$ in the $In_2Se_3/MoS_2$ vdW heterostructure which exceeds that of thin-film silicon devices. The results confirm that the ferroelectric $In_2Se_3/MoS_2$(I) heterostructure is promising for the application to next generation optoelectronic devices.

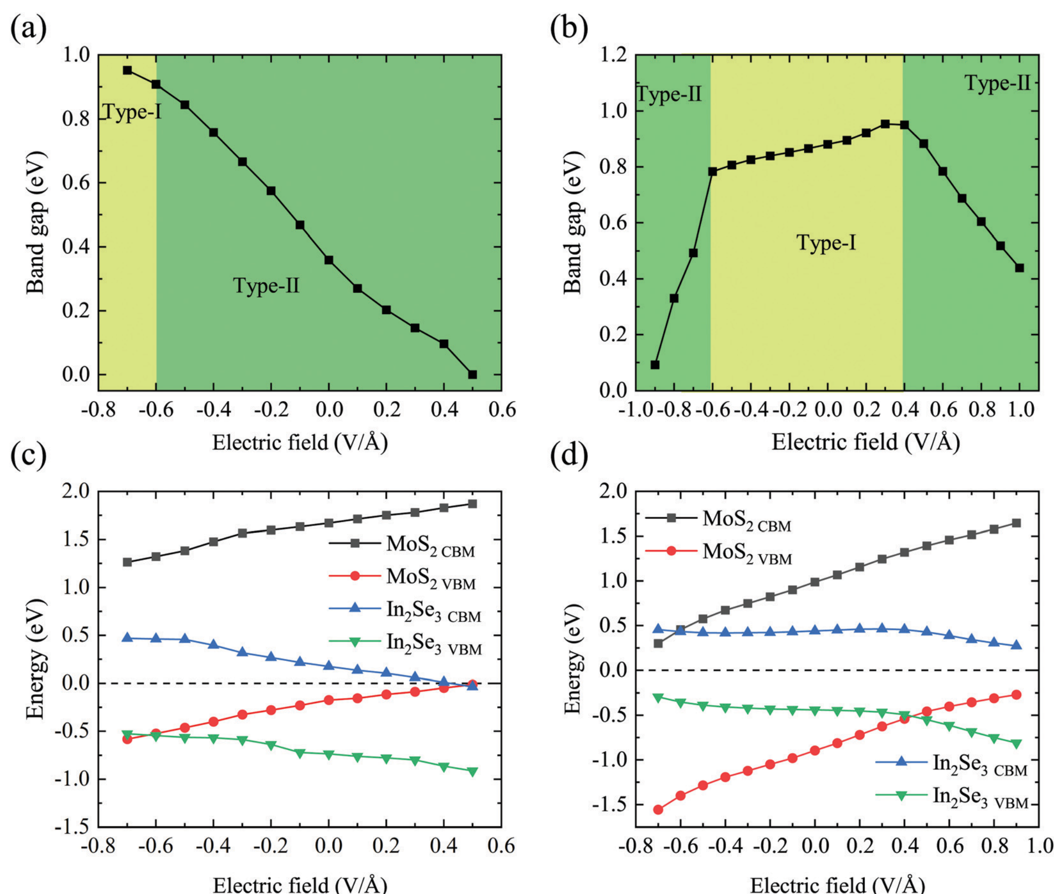


Fig. 6 The evolution of band gap and band edge as a function of $E_{ext}$ in $In_2Se_3/MoS_2$(I) (a and c) and $In_2Se_3/MoS_2$(III) (b and d).

Published on 29 June 2020. Downloaded by East China Normal University on 8/25/2020 1:25:02 PM.

### 3.4 Electric field effects on electronic properties of $In_2Se_3$/$MoS_2$ heterostructures

To investigate the device potentials of $In_2Se_3$/$MoS_2$, it is quite necessary to investigate their band offsets under the effect of an external electric field ($E_{ext}$). Here, we consider the $E_{ext}$ perpendicular to the $In_2Se_3$/$MoS_2$ sheet, the positive direction of the $E_{ext}$ is defined as pointing from the $In_2Se_3$ layer to the $MoS_2$ layer. In Fig. 5, we present the projected band structures of $In_2Se_3$/$MoS_2$(I) and $In_2Se_3$/$MoS_2$(III) with a series of different $E_{ext}$. We can see that when the $E_{ext}$ is $-0.7$ V Å$^{-1}$, the VBM of $MoS_2$ is slightly higher than that of $In_2Se_3$, which embodies the performance of a classic type-I band alignment, as shown in Fig. 5(a). Then, $In_2Se_3$/$MoS_2$(I) retains type-II band alignment characteristics under the $E_{ext}$ of $-0.5$ V Å$^{-1}$ or 0.3 V Å$^{-1}$, in which the CBM is contributed by $In_2Se_3$ and VBM is contributed by $MoS_2$. As the exterior $E_{ext}$ further increases to 0.5 V Å$^{-1}$, the heterostructure will possess the typical characteristics of a metal and the band gap vanishes. For $In_2Se_3$/$MoS_2$(III), as shown in Fig. 5(b), the type-I band alignment is maintained for the applied $E_{ext}$ of $-0.5$ V Å$^{-1}$ and 0.4 V Å$^{-1}$, in which both the CBM and VBM of the $In_2Se_3$/$MoS_2$(III) are entirely contributed by the $In_2Se_3$ layer. When the positive electric field exceeds 0.4 V Å$^{-1}$, however, the CBM of the $In_2Se_3$/$MoS_2$(III) is provided by $In_2Se_3$ while the VBM is dominated by the $MoS_2$ layer. For the $E_{ext}$ at $-0.7$ V Å$^{-1}$, the situation is the opposite, the CBM and VBM of the $In_2Se_3$/$MoS_2$ are provided by $MoS_2$ and $In_2Se_3$, respectively, which show a distinct type-II band alignment.

Fig. 6 shows the evolution of band gaps and band edges for $In_2Se_3$/$MoS_2$(I) and $In_2Se_3$/$MoS_2$(III) heterostructures. It can be seen from Fig. 6(a) that when the $E_{ext}$ is loaded from $-0.7$ V Å$^{-1}$ to 0.5 V Å$^{-1}$ for $In_2Se_3$/$MoS_2$(I), the band gap decreases almost linearly from a maximum of 0.98 eV to 0 eV. For $In_2Se_3$/$MoS_2$(III), as shown in Fig. 6(b), the band gap reaches the maximum value of 0.95 eV at 0.4 V Å$^{-1}$, and then it decreased almost linearly to 0.5 eV at 0.9 V Å$^{-1}$. While when the $E_{ext}$ is loaded below 0.4 V Å$^{-1}$, the band gap firstly decreased slowly from 0.95 eV to 0.78 eV at $-0.6$ V Å$^{-1}$, then it rapidly reduced to 0.1 eV at $-0.9$ V Å$^{-1}$. In Fig. 6(c) and (d), the band edges of $In_2Se_3$ and $MoS_2$ for configurations I and III are presented with respect to their Fermi level. With the applied $E_{ext}$, the band edge positions of $MoS_2$ increased linearly while the band edge of $In_2Se_3$ almost shows a linearly decrease in $In_2Se_3$/$MoS_2$(I). Similar behavior also appears for the $In_2Se_3$/$MoS_2$(III) heterostructure. All these novel findings indicate that electrostatic gating can provide an effective control over the band structures and electronic properties of the heterostructure, which makes the $In_2Se_3$/$MoS_2$ heterostructure become a good candidate for applications in optoelectronic detectors and FETs.

## 4 Conclusions

In summary, we have systematically investigated the electronic properties of the $In_2Se_3$/$MoS_2$ heterostructure with three configurations through first-principles calculations. The results show that the bandstructures of $In_2Se_3$/$MoS_2$ highly depend on the intrinsic ferroelectric polarization of $In_2Se_3$. The band alignment of $In_2Se_3$/$MoS_2$ switches from type-II to type-I, when the ferroelectric polarization of $In_2Se_3$ is reversed from downward to upward. Besides, the calculated photoinduced current density under visible-light radiation is up to 0.5 mA cm$^{-2}$ in the $In_2Se_3$/$MoS_2$ vdW heterostructure and is exceeding that of thin-film silicon devices. Moreover, the controllable band alignment also can be realized through the application of an external electric field. The present results indicate that the $In_2Se_3$-based polarization vdW heterostructure would provide new degrees of freedom in band engineering and is expected to yield novel multifunctional semiconductor heterostructures with tunable optoelectronic properties.

## Conflicts of interest

There are no conflicts to declare.

## Acknowledgements

This work was financially supported by the National Key Research and Development Program of China (Grants No. 2018YFB0406500, 2017YFA0303403, and 2019YFB2203400), the National Natural Science Foundation of China (Grants No. 91833303, 61974043, 61774059, and 61674057), Projects of Science and Technology Commission of Shanghai Municipality (Grant No. 18JC1412400, 18YF1407200, 18YF1407000, and 19511120100), and the Program for Professor of Special Appointment (Eastern Scholar) at Shanghai Institutions of Higher Learning.

## References

1 F. Xia, H. Wang, D. Xiao, M. Dubey and A. Ramasubramaniam, *Nat. Photonics*, 2014, **8**, 8511–8516.
2 S. Matsuo, A. Shinya, T. Kakitsuka, K. Nozaki, T. Segawa, T. Sato, Y. Kawaguchi and M. Notomi, *Nat. Photonics*, 2010, **4**, 648.
3 D. Akinwande, N. Petrone and J. Hone, *Nat. Commun.*, 2014, **5**, 1–12.
4 S.-J. Gong, C. Gong, Y.-Y. Sun, W.-Y. Tong, C.-G. Duan, J.-H. Chu and X. Zhang, *Proc. Natl. Acad. Sci. U. S. A.*, 2018, **115**, 8511–8516.
5 C. H. Ahn, K. M. Rabe and J. M. Triscone, *Science*, 2004, **303**, 488–491.
6 W. Ding, J. Zhu, Z. Wang, Y. Gao, D. Xiao, Y. Gu, Z. Zhang and W. Zhu, *Nat. Commun.*, 2017, **8**, 14956.
7 Y. Zhou, D. Wu, Y. Zhu, Y. Cho, Q. He, X. Yang, K. Herrera, Z. Chu, Y. Han and M. C. Downer, *Nano Lett.*, 2017, **17**, 5508–5513.
8 C. Cui, W. J. Hu, X. Yan, C. Addiego, W. Gao, Y. Wang and X. Zhang, *Nano Lett.*, 2018, **18**, 1253–1258.
9 C. Zheng, L. Yu, L. Zhu, J. L. Collins, D. Kim, Y. Lou, C. Xu, M. Li, Z. Wei and Y. Zhang, *Sci. Adv.*, 2018, **4**, eaar7720.
10 K. S. Novoselov, A. Mishchenko, A. Carvalho and A. C. Neto, *Science*, 2016, **353**, aac9439.


This journal is © The Royal Society of Chemistry 2020

Published on 29 June 2020. Downloaded by East China Normal University on 8/25/2020 1:25:02 PM.

11 J. Kang, S. Tongay, J. Zhou, J. Li and J. Wu, *Appl. Phys. Lett.*, 2013, **102**, 012111.
12 D. L. Duong, S. J. Yun and Y. H. Lee, *ACS Nano*, 2017, **11**, 11803–11830.
13 E. Pomerantseva and Y. Gogotsi, *Nat. Energy*, 2017, **2**, 1–6.
14 H. Fang, C. Battaglia, C. Carraro, S. Nemsak, B. Ozdol, J. S. Kang, H. A. Bechtel, S. B. Desai, F. Kronast, A. A. Unal, G. Conti, C. Conlon, G. K. Palsson, M. C. Martin, A. M. Minor, C. S. Fadley, E. Yablonovitch, R. Maboudian and A. Javey, *Proc. Natl. Acad. Sci. U. S. A.*, 2014, **111**, 6198–6202.
15 S. Wan, Y. Li, W. Li, X. Mao, W. Zhu and H. Zeng, *Nanoscale*, 2018, **10**, 14885.
16 Y. Jiang, Q. Wang, L. Han, X. Y. Zhang, L. X. Jiang, Z. Z. Wu, Y. Q. Lai, D. Z. Wang and F. Y. Liu, *Chem. Eng. J.*, 2019, **358**, 752–758.
17 L. L. Kang, P. Jiang, H. Hao, Y. H. Zhou, X. H. Zheng, L. Zhang and Z. Zeng, *Phys. Rev. B: Condens. Matter Mater. Phys.*, 2020, **101**, 014105.
18 G. Kresse and J. Hafne, *Phys. Rev. B: Condens. Matter Mater. Phys.*, 1993, **47**, 558.
19 P. E. Blöchl, *Phys. Rev. B: Condens. Matter Mater. Phys.*, 1994, **50**, 17953–17979.
20 G. Kresse and J. Furthmuöller, *Phys. Rev. B: Condens. Matter Mater. Phys.*, 1996, **54**, 11169–11186.
21 J. P. Perdew, K. Burke and M. Ernzerhof, *Phys. Rev. Lett.*, 1996, **77**, 3865.
22 T. Kerber, M. Sierka and J. Sauer, *J. Comput. Chem.*, 2008, **29**, 2088–2097.
23 S. Grimme, J. Antony, S. Ehrlich and H. Krieg, *J. Chem. Phys.*, 2010, **132**, 154104.
24 H. J. Monkhorst and J. D. Pack, *Phys. Rev. B: Condens. Matter Mater. Phys.*, 1976, **13**, 5188.
25 S. Smidstrup, T. Markussen, P. Vancraeyveld, J. Wellendorff, J. Schneider, T. Gunst, B. Verstichel, D. Stradi, P. A. Khomyakov, U. G. Vej-Hansen, M.-E. Lee, S. T. Chill, F. Rasmussen, G. Penazzi, F. Corsetti, A. Ojanpera, K. Jensen, M. L. N. Palsgaard, U. Martinez, A. Blom, M. Brandbyge and K. Stokbro, *J. Phys.: Condens. Matter*, 2020, **32**, 15901.
26 J. Chen, Y. Hu and H. Guo, *Phys. Rev. B: Condens. Matter Mater. Phys.*, 2012, **85**, 155441.
27 C. Rivas, R. Lake, G. Klimeck, W. R. Frensley, M. V. Fischetti, P. E. Thompson, S. L. Rommel and P. R. Berger, *Appl. Phys. Lett.*, 2001, **78**, 814.
28 M. Palsgaard, T. Markussen, T. Gunst, M. Brandbyge and K. Stokbro, *Phys. Rev. Appl.*, 2018, **10**, 014026.
29 B. J. Huang, P. E. Yang, Y. P. Lin, B. Y. Lin, H. J. Chen, R. C. Lai and J. S. Cheng, *Sol. Energy*, 2011, **85**, 388.
30 A. Splendiani, L. Sun, Y. Zhang, T. Li, J. Kim, C. Y. Chim and F. Wang, *Nano Lett.*, 2010, **10**, 1271–1275.
31 K. F. Mak, C. Lee, J. Hone, J. Shan and T. F. Heinz, *Phys. Rev. Lett.*, 2010, **105**, 136805.
32 C. Xia, W. Xiong, J. Du, T. Wang, Y. Peng and Z. Wei, *Small*, 2018, **14**, 1800365.
33 P. V. Lukashev, T. R. Paudel, J. M. López-Encarnación, S. Adenwalla, E. Y. Tsymbal and J. P. Velev, *ACS Nano*, 2012, **6**, 9745–9750.
34 A. Ramasubramaniam, D. Naveh and E. Towe, *Phys. Rev. B: Condens. Matter Mater. Phys.*, 2011, **84**, 205325.
35 L. Debbichi, O. Eriksson and S. Lebègue, *J. Phys. Chem. Lett.*, 2015, **6**, 3098–3103.
36 T. Ayadi, L. Debbichi, M. Badawi, M. Said, H. Kim, D. Rocca and S. Lebègue, *Phys. E*, 2019, **114**, 113582.
37 Q. J. Wang, Q. H. Tan, Y. K. Liu, C. Qing, X. B. Feng and D. P. Yu, *Phys. Status Solidi B*, 2019, **256**, 1900194.
38 B. Zhou, S. J. Gong, K. Jiang, L. P. Xu, L. Q. Zhu, L. Y. Shang, Y. W. Li, Z. G. Hu and J. H. Chu, *J. Phys.: Condens. Matter*, 2019, **32**, 055703.
39 G. Henkelman, A. Arnaldsson and H. Jonsson, *Comput. Mater. Sci.*, 2006, **36**, 354–360.
40 X. Li, Z. Li and J. Yang, *Phys. Rev. Lett.*, 2014, **112**, 018301.
41 M. Palsgaard, T. Gunst, T. Markussen, K. S. Thygesen and M. Brandbyge, *Nano Lett.*, 2018, **18**, 7275–7281.